RESEARCH ARTICLE

Journal
American Ceramic Society

Porous alkali-activated material from hypergolic coal gangue by microwave foaming for methylene blue removal

Xinyu Li[1] | **Lei Liu**[1] | **Chengying Bai**[1] | **Kun Yang**[1] | **Ting Zheng**[1] | **Shuang Lu**[2] | **Hongqiang Li**[3] | **Yingjie Qiao**[1] | **Paolo Colombo**[4,5]

[1]Key Laboratory of Superlight Materials and Surface Technology, Ministry of Education, College of Materials Science and Chemical Engineering, Harbin Engineering University, Harbin, China

[2]School of Civil Engineering, Harbin Institute of technology, Harbin, China

[3]College of Civil Engineering, Hunan University, Changsha, China

[4]Department of Industrial Engineering, University of Padova, Padova, Italy

[5]Department of Materials Science and Engineering, The Pennsylvania State University, University Park, Pennsylvania, USA

Correspondence
Chengying Bai and Yingjie Qiao, Key Laboratory of Superlight Materials and Surface Technology, Ministry of Education, College of Materials Science and Chemical Engineering, Harbin Engineering University, 150001 Harbin, China.
Email: chengyingbai@hrbeu.edu.cn; chengyingbai@163.com and qiaoyingjie@hrbeu.edu.cn

Abstract
Overall, 100% hypergolic coal gangue (HCG)-based geopolymer foams were produced by a novel saponification-microwave foaming combined route. Microwave foaming with and without expired vegetable oil was first used to produce CG-based geopolymer foams. Macropores were mainly generated by microwave foaming, and mesopores were mainly obtained by the addition of expired soybean oil that underwent a saponification reaction. The effects of the oil content on the density, porosity, pore morphology, compression strength, and methylene blue adsorption properties were studied. High total porosity (85.9–89.0 vol%) and acceptable compression strength (0.46–1.1 MPa) HCG-based geopolymer foams were produced. Foams with 12.59 wt% oil exhibited the best adsorption properties, with an adsorption capacity up to 9.4 mg/g and high removal efficiency of about 95.3%. These solid-waste-based porous components are promising monolithic adsorbents for wastewater treatment.

KEYWORDS
adsorbents, expired oil, hypergolic coal gangue, microwave foaming, porous alkali-activated material

1 | INTRODUCTION

Coal gangue (CG), a residue with lower carbon content than coal discharged during mining, washing, and the processing of coal tunneling, accounts for ~10%–15% of unprocessed coal harvest.[1–3] Owing to the rapid growth of the coal mining industry, the total amount of CG is rising sharply and gradually becoming one of the most significant industrial solid residues; global CG production was about 0.7–1.5 billion tons in 2020.[4] According to the Guizhou Energy Administration, owing to the rapid expansion of coal production capacity, the quality of raw coal in China

has decreased, and the ash content has increased since 2016. At the same time, the degree of coal mining mechanization and the scale of raw coal washing have gradually expanded. Owing to the previously mentioned factors, the output and discharge of CG showed a rapid growth trend from 393 million tons in 2008 to 750 million tons in 2013. The amount of CG produced in China was 729 million tons in 2020,[3] accounting for ∼20% of the total amount of industrial solid waste in the country. However, the comprehensive utilization rate of CG is only about 60%.[5] CG accumulation not only appropriates land but also leads to the contamination of soil, water, and air, causing serious health risks to surrounding residents.[6,7] The temperature and heat content of CG piles tend to increase owing to oxidation, which can trigger the spontaneous combustion of CG, forming hypergolic coal gangue (HCG) minerals.[8] The mineral composition of CG varies greatly because of the complexity and diversity of coal sources. However, the dominant chemical components are SiO_2 and Al_2O_3, which are considered to possess pozzolanic activity, and several other components, such as CaO, Fe_2O_3, MgO, Na_2O, Ti_2O, K_2O, and SO_3.[9] The principal mineralogical components of CG are kaolinite, quartz, and illite.[10] In addition, CG contains metakaolin, which can be activated using alkaline solutions to obtain alkali-activated materials (AAMs).[11]

AAMs synthesized from amorphous aluminosilicate minerals activated by an alkaline solution are cementitious materials with high binding characteristics.[12] In fact, AAMs, developed during the 1950s by Glukhovsky, are considered a new generation of binder materials and have attracted wide interest in recent years.[13] Generally, solid waste from industrial production containing SiO_2 and Al_2O_3 is utilized as an aluminosilicate source to obtain AAMs. Therefore, the production of AAMs offers an opportunity to upcycle a wide range of industrial solid by-products into high-value materials.[14] AAMs are suitable for ceramic formation,[15,16] refractories,[17] fiber-reinforced composites,[18,19] and thermally resistant materials.[20] The introduction of a porous structure not only provides additional functionality to a component but also greatly increases its added value.[21,22] Particularly in the field of water pollution, porous AAMs (PAAMs) show unique advantages as adsorbents because the overall characteristics of porosity (amount of total porosity, pore interconnectivity, pore size, and size distribution) and adsorption characteristics (e.g., specific surface area, number, and type of active sites) can be independently controlled.[23,24] Currently, PAAMs and alkali-activated material foams (AAMFs) are a fast-growing research area

in the field of porous inorganic nonmetal materials, owing to a combination of appropriate morphology[25–27] and functionality.[28–30] Chemical and mechanical foaming[31–34] are the most frequently used approaches for the fabrication of PAAMs, whereas other methods include replica,[35] sacrificial filler,[36–39] and additive manufacturing.[40–42] Previous investigations have shown that cooking oils can be used as in situ surfactants for porous geopolymers, also known as reactive emulsion templating routes, based on a saponification reaction mechanism.[34,43] Waste cooking oil, including frying oil and expired oil, can be reused to produce soap.[43,44] Global waste cooking oil production has increased with population and economic development, and waste cooking oil can be reused as a feedstock for products, such as biodiesel, fuel, detergent, soap, lubricants, polyurethane products, and aromatherapy candles production.[45–47]

Most processing approaches to AAMs require a rather long curing time (on the order of a few days) to ensure adequate strength of the material, and microwave foaming has the potential to avoid this step, simplifying the overall manufacturing process. Indeed, microwave irradiation, where microwave energy penetrates a material interacting at a molecular level,[48] has shown promise, enabling rapid foaming with little or no addition of blowing agents or other pore-forming substances.[49] This approach has mainly been applied to the manufacture of foams from a wide range of materials, such as plastics,[50,51] starch,[52] phenolic resins,[51] and metals.[53] A few studies have also confirmed that microwaves can be used to induce the generation of pores in a geopolymer mortar, which is a subset of AAMs produced from aluminosilicate precursors with a low calcium content.[54–58] In contrast to conventional methods of introducing porosity using a foaming agent, microwave foaming utilizes the free water in a fresh paste as a foaming medium. Several publications have reported the role of sodium silicate and alkalis in the foaming of bottom ash-based geopolymers obtained by microwave irradiation.[55,57] Up to now, density values as low as 0.44 g/cm^3 have been achieved through microwave foaming.[54]

The purpose of this study is to investigate the feasibility of employing microwave foaming for the synthesis of HCG-based PAAMs. Expired soybean oil was introduced as a foam stabilizer to adjust the pore structure, and its effects on the porosity, density, cellular morphology, mechanical properties, and methylene blue (MB) adsorption properties of the foamed samples for potential sewage disposal applications were evaluated.

TABLE 1 Chemical composition of the hypergolic coal gangue (wt%)

SiO$_2$	Al$_2$O$_3$	Fe$_2$O$_3$	K$_2$O	TiO$_2$	MgO	CaO	Na$_2$O	LOI[a]
54.12	28.83	12.22	0.96	0.89	0.80	0.78	0.29	2.62

[a]LOI = loss of ignition at 1000°C.

2 | EXPERIMENTAL SECTION

2.1 | Materials

HCG was generated by the self-ignition of coal gangue owing to heat accumulation. HCG from Dalianhe (Harbin, China) was used as the only source of aluminosilicate mineral material to fabricate PAAMs. Table 1 shows the chemical composition of the HCG, as determined by XRF, indicating that silica and alumina were the main components.

The alkali-activator solution was obtained by mixing a solution of 9.4 M NaOH (by dissolving solid NaOH from Jindong Tianzheng, Tianjin, China in deionized water for at least 24 h at room temperature) with a liquid water glass (sodium silicate solution from Dongyue, Shandong, China, with 8.3 wt% Na$_2$O and 26.5 wt% SiO$_2$ content) using a top-mounted electronic stirrer (OS20-Pro, DragonLab, Beijing, China). Expired oil (Jiusan, Heilongjiang, China) was selected as the precursor for the stabilizing agent (SA), or surfactant.

2.2 | Manufacturing process

Figure 1 shows a flow diagram of the production of PAAMs using the fast microwave foaming method. The starting alkali-activated suspension was prepared by mixing HCG and an alkali-activator solution for 20 min at 500 rpm and ambient temperature. Suspensions with a 40.89 wt% CG content had the following molar ratios: SiO$_2$/Al$_2$O$_3$ = 4.70, Na$_2$O/Al$_2$O$_3$ = 1.21, Na$_2$O/SiO$_2$ = 0.30, and H$_2$O/Na$_2$O = 16.31. Subsequently, expired oil (SAs), defined as x% according to its weight fraction in the solution, was added by mixing at 1000 rpm for 5 min. Samples without oil were used as a reference. After mixing, AAM slurries with different amounts of oil were poured into a silicone mold and covered with a plastic wrap. The samples were then cured as well as foamed in a household microwave oven (G70F23N1L-SD, Galanz, Guangdong, China) at a medium power setting that was modified by the maximum power working time (i.e., 60% working time with maximum power at 750 W and 40% working time without microwave heating) for 5 min, after which the specimens were cured at 75°C in an oven for another 24 h to consolidate the structure and further complete the alkali activation reaction.[59,60] An extraction step, which was aimed at fully eliminating any residual oil and water-soluble substance (i.e., glycerol and soap molecules produced through the saponification reaction), was carried out by saturating the specimens in hot water and changing the water each hour until it became clear.[34,59] The dimensions of the samples were ~15 × 65 × 65 mm^3 after polishing.

2.3 | Characterization

The bulk density (ρ_b) of the samples was determined by the ratio between the weight of a dry parallelepiped specimen and its geometrical volume according to ASTM C20-00. The true density (ρ_t) was assessed using a water pycnometer at a bath temperature of 25°C on finely ground powders as well as powders calcinated at 600°C, according to ASTM C604. The reported values are the average of three measurements. The total void fraction (ε) was computed using the following equation[61]:
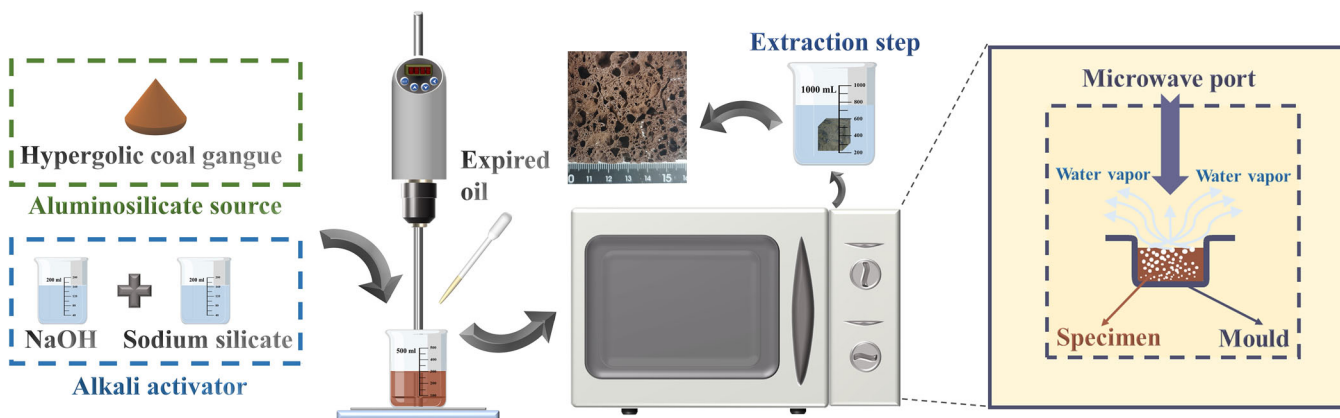
FIGURE 1 Schematic of the synthesis of porous hypergolic coal gangue–based alkali-activated materials (AAMs) produced by the fast microwave foaming method

TABLE 2 Kinetic model parameters (pseudo-first-order [PFO], pseudo-second-order [PSO], and intra-particle diffusion [IPD]) for initial methylene blue (MB) adsorption on porous alkali-activated materials (AAMs)

Sample	$q_{e,exp}$ (mg/g)	PFO		PSO		IPD model	
		$q_{e,cal}$ (mg/g)	R^2	$q_{e,cal}$ (mg/g)	R^2	R_1^2	R_2^2
S0 R0	6.962	1.084	0.041	6.338	0.999	0.396	0.637
S1 R0	5.345	1.737	0.372	5.024	0.991	0.583	0.996
S2 R0	10.333	5.141	0.972	9.000	0.988	0.863	0.941
S3 R0	10.669	3.963	0.859	10.374	0.997	0.728	0.894
S4 R0	9.423	4.519	0.959	9.337	0.996	0.943	0.860
S5 R0	7.623	2.747	0.886	7.530	0.998	0.914	0.938

$$\varepsilon, \text{vol\%} = 100\% \left(1 - \rho_b/\rho_t\right) \quad (1)$$

where ρ_b is the bulk density, and ρ_t is the true density.

Compressive strength tests were performed using a universal testing machine (WDW-100, Kexin, Changchun, China) at a crosshead loading rate of 1 mm/min, and four specimens ($\sim15 \times 20 \times 20$ mm^3) were cut from larger samples to obtain the average compressive strength value and standard deviation. The samples were tested parallel to the foaming direction.

The pore morphology of the cut cross section of the samples was characterized using a Boshida stereo light microscope (BD-61T, Shenzhen, China) with fixed light optical magnification in the range 15 to $\sim200\times$. Selected PAAM samples with and without expired oil were characterized using scanning electron microscopy (SEM, Apreo S LoVac, Thermo Scientific, Madison, USA).

The crystalline phase assemblage of the HCG and selected AAM powders was investigated by X'Pert Pro X-ray powder diffraction (XRD, PANalytical, the Netherlands) using Cu K_α radiation ($\lambda = 1.542$ Å) operated at 40 kV and 40 mA with a 2θ step size of 0.03° and a scan rate of 50 s per step.

The hydration and bonding behavior of the AAMs was characterized using a Nicolet-6700 Fourier-transform infrared spectrophotometer (FTIR, Thermo Scientific, USA). FTIR spectra were recorded using the KBr pellet technique on ground specimens from 500 to 4000 cm^{-1}.

Brunner–Emmett–Teller (BET) surface area and N$_2$ adsorption–desorption isotherms were acquired using a specific surface area analyzer (TriStar II 3020 2.00, Micromeritics, USA). The pore volume, pore size distribution, and average pore size were obtained according to the Barrett–Joyner–Halenda (BJH) analysis using the desorption branch.

2.4 | Adsorption tests

The adsorption of MB by samples produced with different amounts of oil was investigated by stirring 0.2 L of MB solution (40 ppm) with ~0.8 g of foam samples using a magnetic stirrer (S10-3, Sile, Shanghai, China) at room temperature. The stock solution was prepared by dissolving MB (Yousuo, Shandong, China) in deionized water, and the physicochemical characteristics of the MB are reported in Table 2. The MB concentration was determined using an ultraviolet–visible spectrophotometer (UV-2100 PC, Jinghua, Shanghai, China) at a wavelength of 664 nm.

The amount of MB uptake (q) and removal efficiency (E) were computed according to the following equations[62]:

$$q \text{ (mg/g)} = \frac{(C_0 - C_t)}{m} \times V \quad (2)$$

$$E \text{ (\%)} = \frac{(C_0 - C_e)}{C_0} \times 100\% \quad (3)$$

where C_0 and C_t are the MB concentrations (mg/L) at the initial time and at time t, V (L) is the volume of the MB solution, and m (g) is the mass of the porous HCG-based AAM.

The sorption response is time-dependent, and several models, including pseudo-first-order (PFO) kinetic, pseudo-second-order (PSO) kinetic, intra-particle diffusion (IPD), Weber and Morris sorption, and Bohart–Adams and Thomas sorption models, have been proposed to describe adsorption kinetics.[63] The influence of contact time on the amount of MB adsorbed was evaluated, and the adsorption kinetics data were fitted with the PFO (Equation 4), PSO (Equation 5), and IPD models (Equation 6)[64]:

$$\ln\left(q_e - q_t\right) = \ln q_e - k_1 t \quad (4)$$

$$\frac{t}{q_t} = \frac{1}{k_2 q_e^2} + \frac{t}{q_e} \quad (5)$$

$$q_t = k_{id}\, t^{1/2} + C \quad (6)$$

where q_e is the adsorption amount (mg/g) at equilibrium, q_t is the adsorption amount at time t (min), k_1 (min^{-1}), and k_2 (g/(mg min)) are the PFO and PSO rate constants, respectively, and k_{id} (mg/g min$^{1/2}$) and C (mg/g) are the intra-particle diffusion constants in the IPDM.

Among various regeneration/desorption methods (acid, alkali, salt solution, thermal treatment, complex, etc.), thermal regeneration is known as the most effective and economical procedure and has been widely used with AAM/geopolymer adsorbents.[30,65–70] To explore the feasibility of reusing the foamed samples as adsorbents, all AAM monoliths with different amounts of oil content were heated at 5°C/min to 400°C for 2 h in a muffle furnace to thermally degrade MB. The adsorption capacities of the regenerated samples were studied under the same conditions as the initial tests. The regeneration cycle and tests were conducted four consecutive times.[35]

3 | RESULTS AND DISCUSSION

3.1 | X-ray diffraction and infrared spectroscopy analysis

The development of the matrix after alkali activation was investigated by combining XRD and FTIR analyses, and the results are shown in Figure 2. Figure 2A shows the XRD patterns of AAM samples produced without oil (sample S0) and the starting coal gangue (HCG). Sharp diffraction peaks representing quartz (SiO_2, PDF 00-046-1045) and hematite (Fe_2O_3, PDF 00-033-0664), accompanied by a weak peak of muscovite ($KAl_3Si_3O_{10}(OH)_2$, PDF 01-075-0948) and cristobalite (SiO_2, PDF 01-082-0512), were observed in HCG, with a particularly sharp quartz peak at a 2θ value of ~26.6°. The broad halo between 20° and 35° in the X-ray pattern of the AAM indicates the formation of an amorphous sodium aluminosilicate gel (N–A–S–H) during the synthesis of the material.[71,72] As shown in Figure 2A, the main crystalline phases of the HCG and pure AAM powders are essentially identical, with quartz and hematite being the most abundant phases. The density of the peak at ~21.8° is attenuated, possibly due to the synergistic effect of alkali activation and microwave activation as the sodium silicate glass forms.[73–76]

A phase transformation of natural coal gangue upon geopolymerization can be observed in the FTIR spectrum in Figure 2B. The characteristic bands of HCG are similar to those of calcined coal gangue in the literature.[77,78] The characteristic absorption bands at 1091, 797, 778, and 695 cm^{-1} are ascribed to quartz.[79–81] The broad peak at 3441 cm^{-1} is the characteristic of O–H asymmetric stretching (3000–3700 cm^{-1}), which is associated with the formation of hydrated compounds.[72,82,83] The bending vibration of O–H is observed at ~1626 cm^{-1}, indicating the presence of water molecules.[84–86] The strong absorption band at 1091 cm^{-1} corresponds to the antisymmetric stretching vibration of Si–O, whereas the peaks at 797, 778,
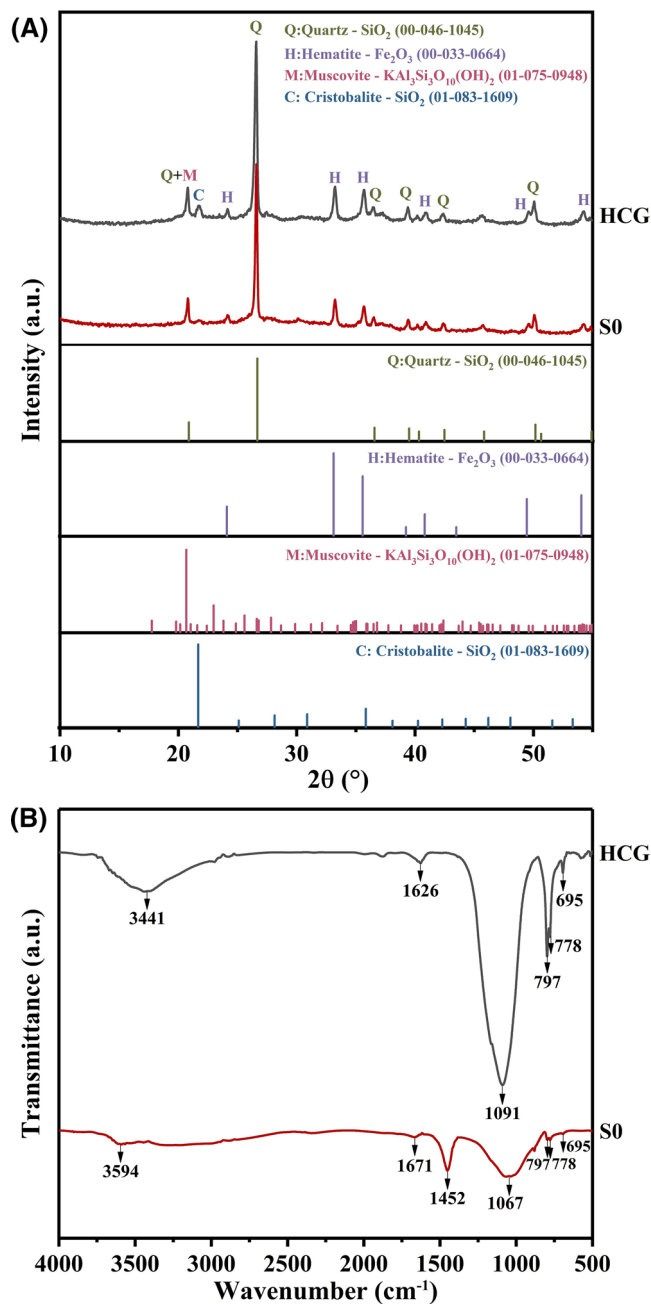

FIGURE 2 X-ray diffraction (XRD) patterns (A) and Fourier-transform infrared (FTIR) spectra (B) of hypergolic coal gangue and alkali-activated material (AAM) powders

and 695 cm^{-1} indicate the presence of the Si–O–Si bond of quartz.[87,88] The band at 797 cm^{-1} can also be attributed to the vibration of sixfold coordinated Al–O, which suggests that the raw powder contains octahedral six-coordinate AlO_6.[89]

After the alkali activation reaction, the sample shows bands at 3594 and 1671 cm^{-1}, which are attributed to O–H from adsorbed atmospheric water.[61] In addition, the peak at 1452 cm^{-1} is assigned to the O–C–O stretching of sodium carbonate formed by the reaction between sodium silicate
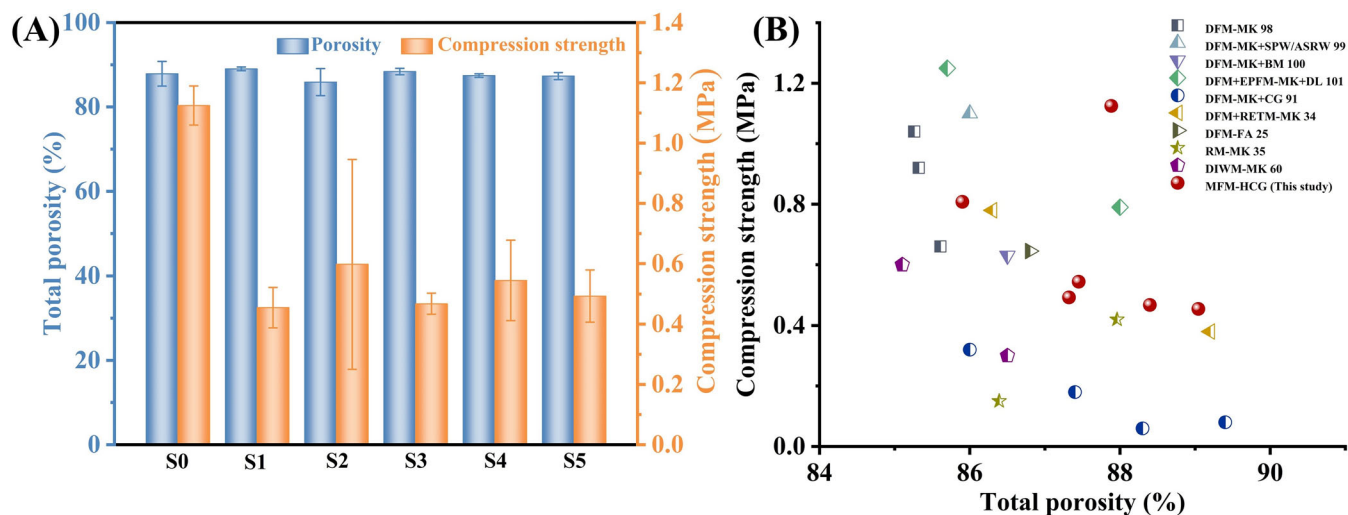
FIGURE 3 (A) Total porosity and compression strength of the porous specimens (S0–S5); (B) the compression strength and the total porosity data of this study (samples S0–S5) (●) and previous data[25,34,35,60,91,98–101] for high-porosity (>85%) samples prepared by different preparation methods. ASRW, aluminum scrap recycling waste; BM, bottom ash; DFM, direct foaming method; DIWM, direct ink writing method; DL, dolomite; EPFM, embedding porous fillers method; FA, fly ash; MFM, microwave foaming method; MK, metakaolin; RETM, reaction emulsion template method; RM, replica method; SPW, steel-plant waste

and air [90,91]. The shift of the Si–O peak located at 1091 cm^{-1} to a lower wavenumber (1067 cm^{-1}) and the broadening of the band which corresponds to the asymmetric stretching vibrations of the Al–O–Si and Si–O–Si bonds [92,93] jointly provide evidence of the occurrence of a geopolymerization reaction.[94,95] As expected, there are no obvious changes in the peaks at 797, 778, and 695 cm^{-1}, attributed to the quartz crystalline phase, which is consistent with the XRD data.

3.2 | Porosity and mechanical strength

Figure 3 and Table S1 show the total porosity (ε, vol%), relative density (ρ_a, g/cm^3), and compression strength (σ, MPa) of the samples with various oil loadings and without oil. There are no significant fluctuations in the ρ_a and ε values, probably because the porosity was generated by microwave foaming and not by frothing (i.e., in situ generation of bubbles rather than the mechanical introduction of gas into the slurry). However, we observed that the introduction of oil into the system led to a strong decrease in the compression strength, independent of its amount. The decrease in σ can likely be explained by a decrease in the alkaline concentration due to the saponification of the oil, leading to the formation of soap molecules and glycerol.[96] Indeed, previous studies[56,34,97] also showed that the alkaline concentration has a significant effect on the σ of samples produced by different foaming routes. Another reason for the observed decrease in strength with the

introduction of oil is related to a change in microstructure, with an increase in the presence of voids within the cell walls and struts when oil is introduced (see Section 3.3). The foams obtained by the combined microwave foaming and reactive emulsion templating route exhibited high total porosity with acceptable compression strength.

3.3 | Pore microstructure

Figure 4 shows optical images of porous specimens prepared with (samples S1–S5) or without (sample S0) oil. A nonhomogeneous cellular structure, also reported in previous studies[56,57,102] concerning microwave foaming, is observed for all samples. The microstructure comprises large cells (0.5 up to 2–5 mm), as shown in Figure 4A,B,D,E,G,H,J,K,M,N,P,Q, and small pores (less than 0.5 mm) present in the cell walls and struts (see Figure 4C,F,I,L,O,R). The number of small pores seems to increase with increasing oil content. The small pores observed in the sample without oil (S0) could be due to inadequate microwave foaming,[56,57] whereas those present in the samples produced with oil (S1–S5) can be explained by the removal of oil droplets and/or the effect of surfactant molecules generated by the saponification reaction. Previous studies of microwave foaming[56,57] suggest that sodium silicate acts not only as an alkaline activating agent but also as a foaming agent, and small pores are also observed in samples produced by the method of direct foaming plus reactive emulsion templating.[34]
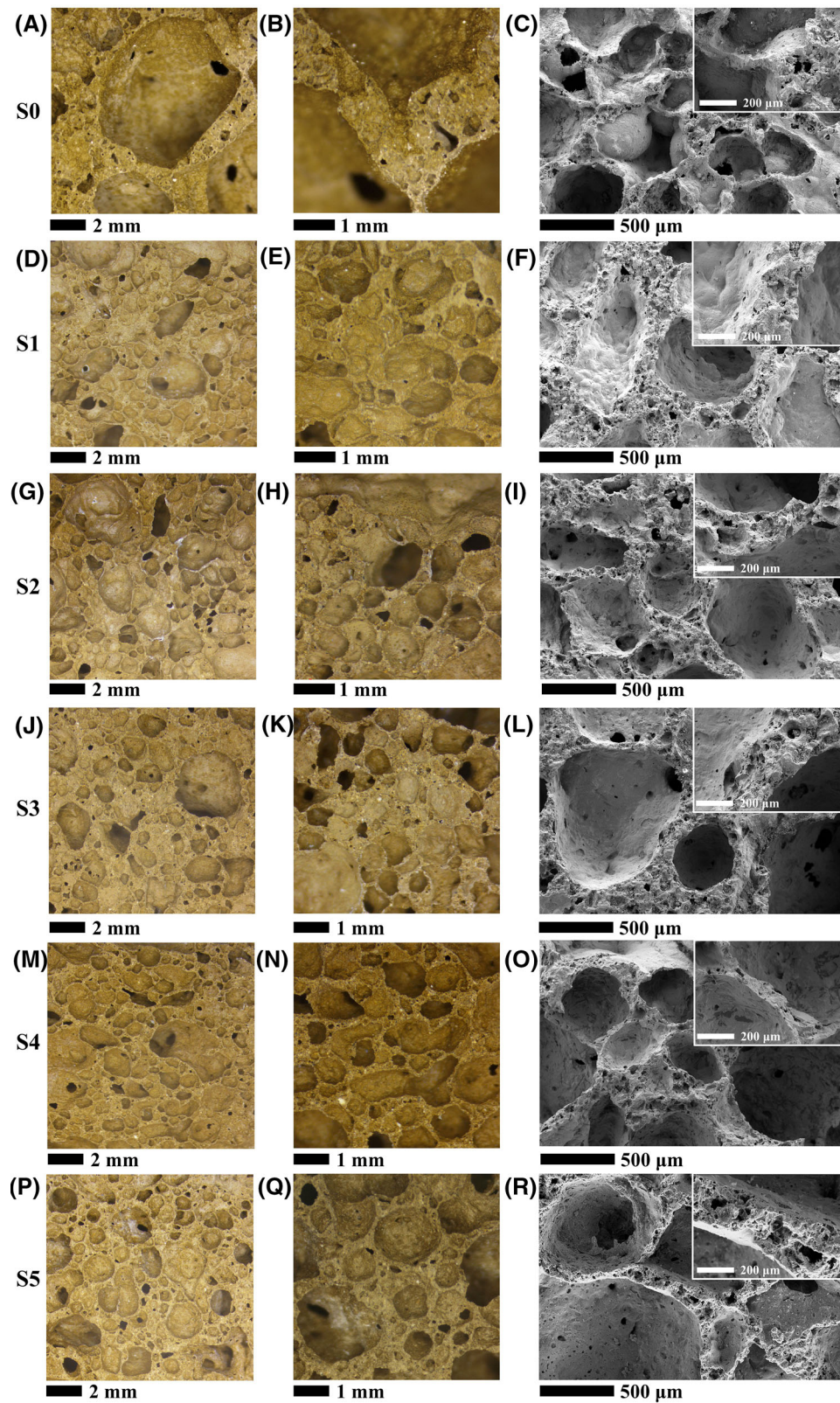
FIGURE 4 Optical images (A, B, D, E, G, H, J, K, M, N, P, and Q) and SEM images (C, F, I, L, O, and R) of porous alkali-activated materials (AAMs) (A, E, I, M, and Q) with various amounts of oil (samples S1–S5) or without oil (sample S0)
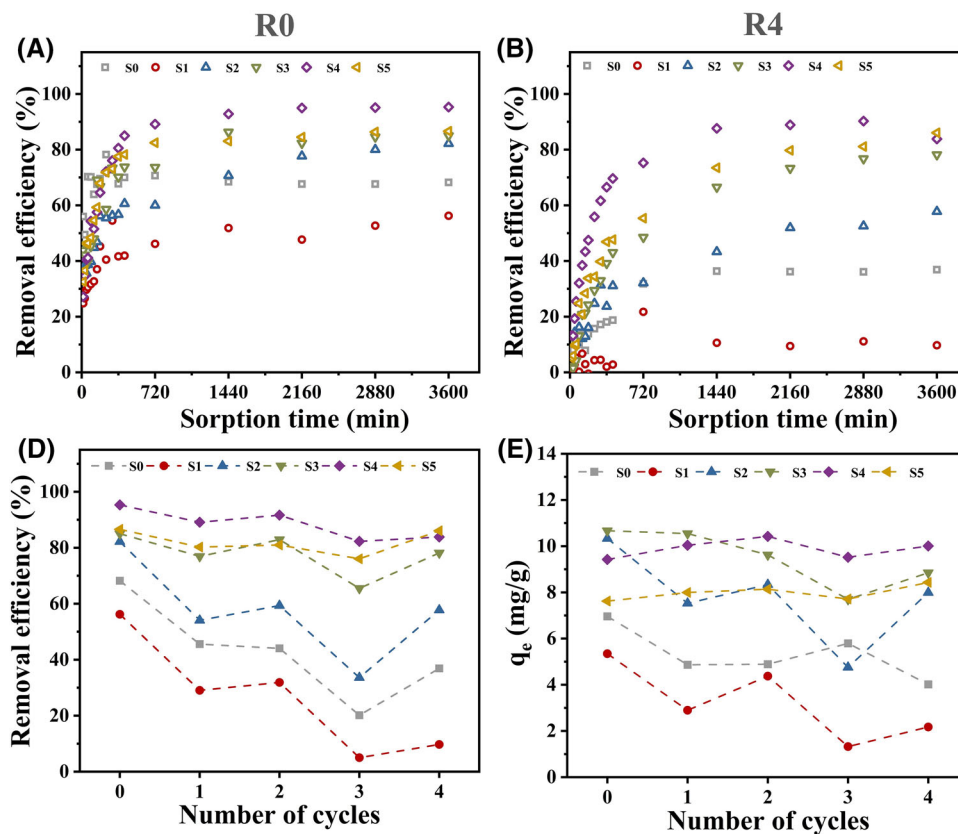
FIGURE 5 Removal efficiency as a function of time of (A) various bulk porous adsorbents (samples S0–S5), and (B) by the same adsorbents after the fourth regeneration cycle; (C) removal efficiency and adsorption amount at equilibrium (q_e); (D) as a function of the regeneration cycle by various bulk porous adsorbents (samples S0–S5)

3.4 | Methylene blue adsorption tests

3.4.1 | Effect of contact time

The time-dependent performance of the absorption of MB from an aqueous phase was assessed on bulk porous adsorbents manufactured with different amounts of oil, on a timescale ranging from 0 to 3600 min, with a fixed MB concentration of 40 mg/L and a constant geopolymer dosage (~0.8 g). A typical trend for the removal efficiency (E) versus contact time, which tracks the adsorption rate, is shown in Figure 5A,B, whereas parts (C) and (D) of Figure 5 show the removal efficiency and the adsorption amount at equilibrium as a function of the number of regeneration cycles, respectively.

It is evident that the adsorption efficiency of MB on the PAAMs increased with the sorption time. Significant MB adsorption occurred within the first 720 min, owing to the availability of more active adsorption sites on the porous adsorbents at the beginning of adsorption. Previous studies[103,104] demonstrated that the adsorption capacity is mainly determined by the ion exchange of Na^+ in PAAM networks with MB molecules and interaction of the

sorbent with the adsorption active sites (hydroxyl groups [−OH] connected to the Si tetrahedra).

During the initial cycle, the MB removal rate gradually decreased with increasing adsorption time as a result of the reduction of active sites. In addition, the removal efficiency (E) reached an equilibrium level (>80% for some samples) at ~720 min and then remained virtually constant up to 60 h of testing. At this equilibrium time, the value of E for some samples was as high as 95.3%, and a similar value was also reached even after four regeneration cycles. Therefore, regeneration had a limited effect on removal efficiency, simply prolonging the time required to achieve adsorption equilibrium.

3.4.2 | Kinetics of adsorption

The adsorption of MB was analyzed using time- and concentration-dependent models that represent adsorption kinetics. Several models have been reported for describing the kinetics of solid–liquid adsorption to investigate the rate-limiting step of the sorption process. Based on the initial MB adsorption data, three major models
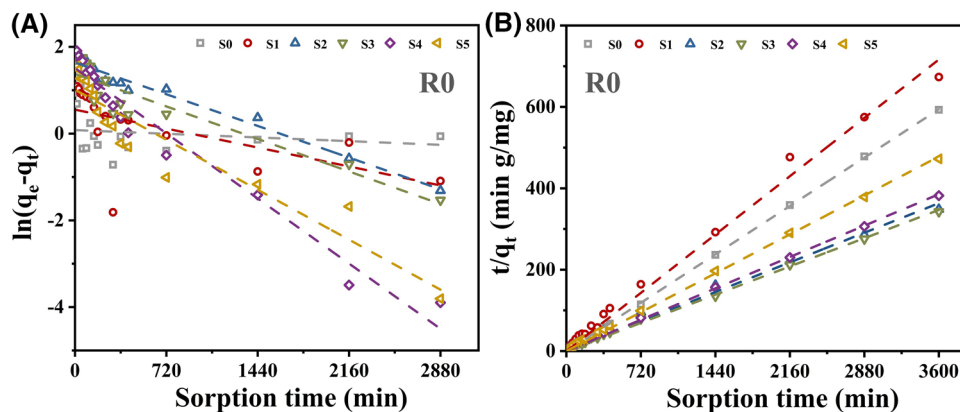
FIGURE 6 (A) Pseudo-first-order kinetic plot and (B) pseudo-second-order kinetic plot for initial methylene blue (MB) adsorption

(PFO, PSO, and IPD) were applied, using linear regression analysis to determine the fit of the models.

The fitting of the MB adsorption experimental data is shown in Figures 6 and S1, and the corresponding kinetic adsorption parameters, the correlation coefficients (R^2), and the calculated adsorption amount ($q_{e,cal}$) are reported in Table 2. As seen in Table 2, the R^2 of the PFO kinetic model was between 0.041 and 0.959, that of the IPD model was between 0.396 and 0.996, whereas that of the PSO kinetic model was between 0.988 and 0.999 with most R^2 values greater than 0.99. This demonstrates that the PSO model best fits the experimental data. In addition, $q_{e,cal}$ of the PSO kinetic model was in close agreement with the experimental value ($q_{e,exp}$). Therefore, we posit that the adsorption of MB was dominated by chemisorption, and the addition of oil did not significantly change the solid–liquid adsorption mechanism in the materials. Similar behavior was reported for the adsorption kinetics of MB onto geopolymers,[105–107] spent tea leaves,[108] and oil palm (*Elaeis guineensis*).[109]

3.4.3 | Effect of oil content

Figure 7A,B shows the E and Q_t values of the foam samples as a function of the amount of oil. It was rather surprising to observe that the MB uptake and Q_t by the PAAMs significantly increased with an increase in oil content for all the specimens except S1. Apparently, a limited addition (3.14 wt%) of oil reduced the adsorption capacity of the foams, with decreases in E and Q_t of 28.1% and 23.2%, respectively. However, the adsorption performance was significantly enhanced when the oil content was raised to 6.29 wt%, and in particular, the adsorption capacity was increased by 48.4%, to almost the same as the maximum value of 10.7 mg/g (S3). Moreover, the addition of oil distinctly promoted the removal efficiency. For example, a 21.8% increase in the MB removal efficiency was observed

for sample S4 when the amount of oil increased from 0% to 12.59%. The very high MB removal efficiency (95.3%) of S4 revealed a strong interaction between the available MB molecules in solution and the AAM active sites. The positive effect of the use of oil during the manufacture of the samples remained after four regeneration cycles, and the Q_t values of samples S4 and S5 remained almost unchanged. In particular, the specimen with 12.59% oil (S4) exhibited the best adsorption performance.

Samples with and without oil (S4 and S0) were subjected to nitrogen adsorption–desorption tests to understand the effect of oil on the BET surface area as well as the BJH desorption average pore size and pore volume (see Table 2). The addition of oil did not significantly change the nitrogen adsorption–desorption isotherms (see Figure 8A,C), which were all type IV and presented a vertical asymptotic profile at high values of P/P_0.[110] In addition, the type H3 hysteresis loops suggest that the pores are nearly slit-like.[95,111] Initially, the monolayer changed to a multilayer on the pore surface, displaying a plateau at medium–low pressure ($P/P_0 = 0.2$–0.8).[112,113] The sample synthesized without oil (S0) possessed mesopores with an average dimension of 2.4 nm and macropores with a broad size distribution from 10 to 260 nm, with a single peak centered at 121 nm. With the addition of oil, the small mesopores (2.4 nm) disappeared, and the number of larger pores, with sizes between 20 and 40 nm, gradually increased. This is consistent with the observed difference in pore volume in the samples, with that for S4 sample (0.029 cm³/g) being 10 times larger than that of the S0 sample (0.003 cm³/g), while the surface area and average pore size decreased (see Table 3). The larger pore volume developed with the help of oil provided numerous additional active sites capable of binding to the MB molecule.

Table 4 compares the MB uptake (Q_e) and removal (E) of various foams (bulk-type adsorbents) reported in the literature. The maximum MB removal efficiency (95.3%) was higher than that of several other adsorbents but lower
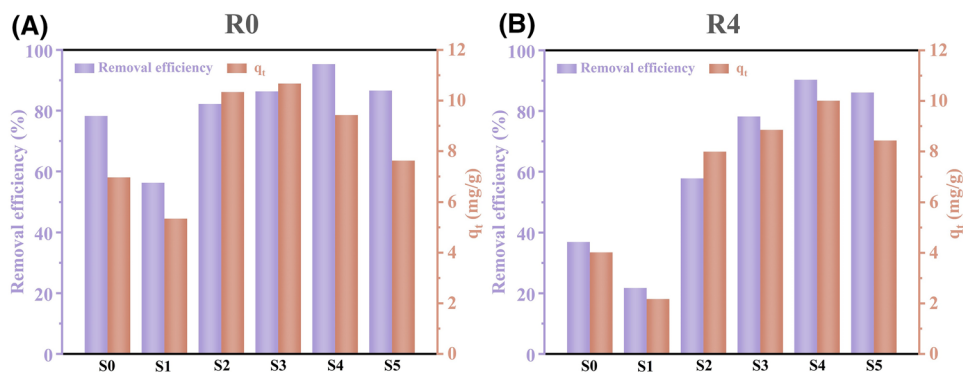
FIGURE 7 E and Q_t values for methylene blue (MB) adsorption on porous samples (as received) manufactured with different amounts of oil (samples S0–S5) (A), and after the fourth regeneration cycle (B)
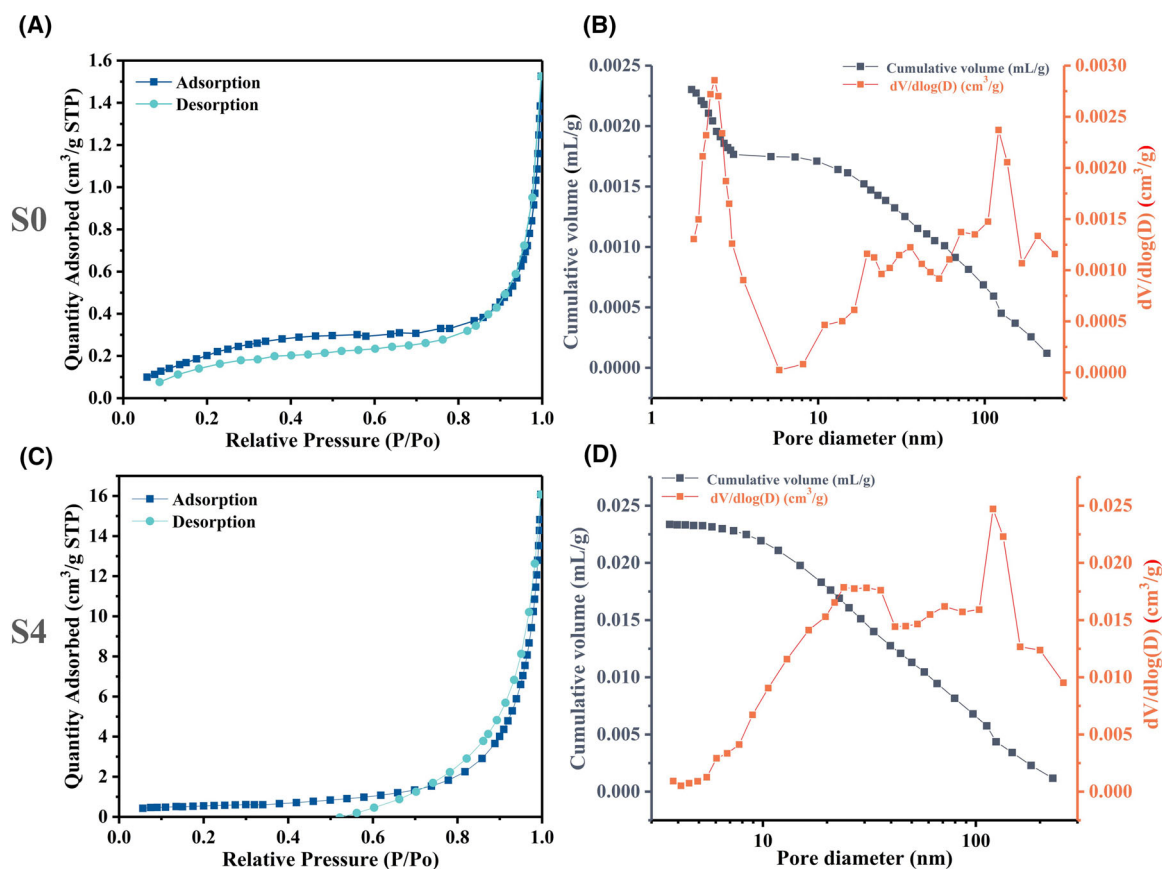

FIGURE 8 N_2 adsorption–desorption curve (A and C), pore size distributions and cumulative pore volume (B and D) of selected porous alkali-activated materials (AAMs) (samples S0, S4)

TABLE 3 Brunner–Emmett–Teller (BET) surface area, Barrett–Joyner–Halenda (BJH) desorption pore volume, and BJH desorption average pore size of selected samples (S0, S4)

Sample	BET surface area (m²/g)	BJH desorption pore volume (cm³/g)	BJH desorption average pore size (nm)
S0	0.9442	0.002686	9.8909
S4	1.8904	0.028585	20.5017

than that of metakaolin/glass geopolymers.[104] However, the maximum MB uptake here (9.4 mg/g) was much better than that reported by Rożek et al.,[104] as a cumulative adsorption amount of 49.4 mg/g was reached. These data illustrate the tremendous potential of our samples as innovative monolithic adsorbents that can be directly applied in the form of packed beds.

TABLE 4 Methylene blue (MB) uptake (Q_e) and removal (E) of various foams (bulk-type adsorbents) reported in the literature (uptake (Q_e) was extrapolated from the experimental data)

Raw material	Adsorbent shape	C_0 (ppm)	Q_e (mg/g)	E (%)	Ref.
Metakaolin + biomass fly ash	Disc (d = 22 mm; h = 3 mm)	50	15.4 (1st) 109.6 (6th)	64.8 (1st) 48.4 (6th)	114
Bauxite residue	Disc (d = 20 mm; h = 3 mm)	50	17.3 (1st) 39.2 (5th)	17.3 (1st) 39.2 (5th)	65
Metakaolin + glass	Monolithic (15 × 15 × 5 mm)	50	4.9 (1st)	~100 (1st)	104
Coal fly ash	–	50	2.97 (1st)	–	115
Hypergolic coal gangue	**Monolithic (25 × 15 × 5 mm)**	**40**	**9.4 (1st) 49.4 (4th)**	**95.3 (1st) 83.9 (4th)**	**This study (S4)**
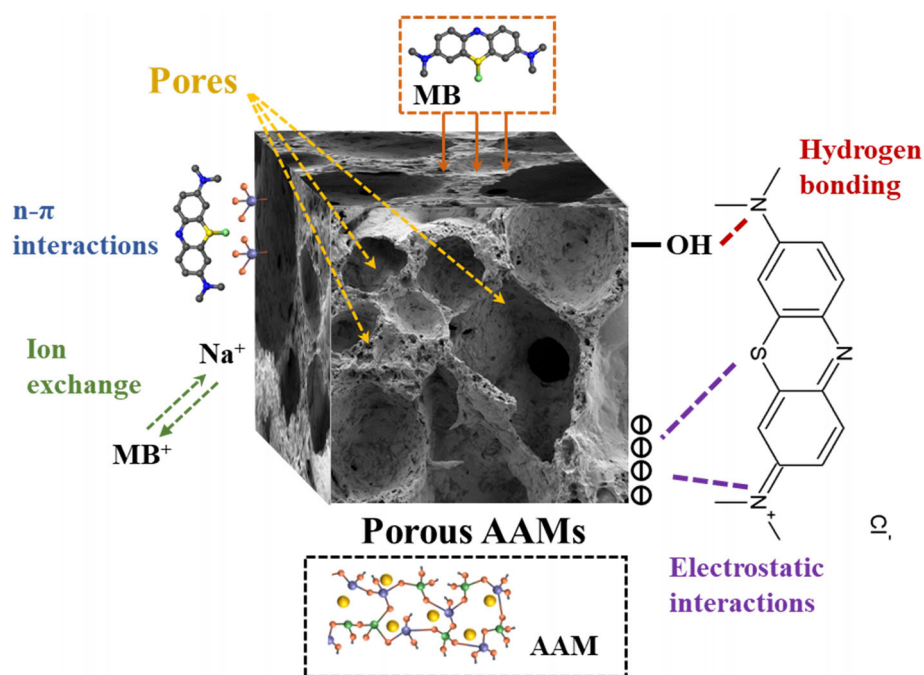
FIGURE 9 Proposed adsorption mechanisms of methylene blue (MB) on hypergolic coal gangue (HCG)-based porous alkali-activated materials (AAMs)

3.4.4 | Regeneration tests

All specimens manufactured using different oil contents were used for five adsorption experiments (including the initial adsorption) and were regenerated by thermal treatment at 400°C to promote the thermal decomposition of the adsorbed MB. The results of the regeneration tests are shown in Figure 5C,D.

After the first regeneration, a decrease in MB removal efficiency and a loss in uptake were observed compared with the initial adsorption test in the great majority of specimens, highlighting the negative impact of the heat treatment, which was almost inevitable. This decline can be explained by a decrease in the number of active sites due to mass loss and incomplete degradation[30] of MB after thermal treatment. However, a rebound in the adsorption performance was observed after the second cycle, which is related to an increase in porosity caused by the heat treatment.[114] Subsequently, a slight reduction in the MB uptake of the samples was observed. Nevertheless, the decrease in MB absorption and removal efficiency was relatively minor, clearly demonstrating stable adsorption behavior after multiple regeneration cycles. Surprisingly, the samples produced with the addition of oil could

withstand the negative effects of heat treatment, at least to a certain extent. The adsorption amount of S4 was slightly superior to that without regeneration (from 9.4 to 10.0 mg/g), demonstrating the possibility of reusing this innovative adsorbent for wastewater treatment.

3.4.5 | Adsorption mechanism

MB adsorption onto PAAMs in an MB solution involves the following steps: MB molecules migrate from the solution to PAAMs; MB molecules diffuse through the boundary layer to the surface of the PAAMs; MB molecules are adsorbed onto the active sites of the surface; and MB molecules diffuse to the inner pores of the adsorber.[105,116] Figure 9 shows the adsorption mechanism of MB on PAAMs. The possible adsorption mechanisms associated with MB onto PAAMs can be explained considering several aspects. The first aspect is the ion exchange properties of MB cations and Na^+ charge-balancing cations in the PAAM network.[117,118] The second is related to $n–\pi$ interactions between the structure of PAAMs and the MB-conjugated structure.[117,118] A third aspect takes into account the electrostatic interactions between the positively charged sites of MB^+ and the negatively charged tetrahedral Al sites.[86,105] Finally, hydroxyl groups ($-OH$) attract the N or S atoms of the MB dye to form hydrogen bonds.[69,119]

4 | CONCLUSIONS

Porous HCG-based AAMs were manufactured for the first time with the addition of expired soybean oil using a novel combined saponification/microwave foaming route. The following points can be made in summary:

1. The produced foams exhibited high total porosity (85.9–89.0 vol%) and acceptable compression strength (0.46–1.1 MPa).
2. Increasing the oil content caused a decrease in the compression strength, but a substantial increase in the adsorption characteristics. Adsorption capacity up to 9.4 mg/g and a high removal efficiency about 95.3% for MB were realized. There was no significant decrease in the adsorption properties after 1–4 regeneration cycles.
3. Foams with coal gangue (100 wt%) as the raw mineral material can be employed as adsorbing components for wastewater treatment, providing a novel strategy for upcycling solid waste and expired oil.

The online version of this article contains supplementary materials (Table S1 and Figure S1), which are available to authorized users.

CONFLICT OF INTEREST

The authors declare that they have no conflict of interest.

ORCID

Chengying Bai https://orcid.org/0000-0003-2555-2330
Paolo Colombo https://orcid.org/0000-0001-8005-6618

REFERENCES

1. Dong Y, Di J, Yang Z, Zhang Y, Wang X, Guo X, et al. Study on the effectiveness of sulfate-reducing bacteria combined with coal gangue in repairing acid mine drainage containing Fe and Mn. Energies. 2020;13(4):995. https://doi.org/10.3390/en13040995
2. Qureshi AA, Kazi TG, Baig JA, Arain MB, Afridi HI. Exposure of heavy metals in coal gangue soil, in and outside the mining area using BCR conventional and vortex assisted and single step extraction methods. Impact on orchard grass. Chemosphere. 2020;255:126960. https://doi.org/10.1016/j.chemosphere.2020.126960
3. Li J, Wang J. Comprehensive utilization and environmental risks of coal gangue: a review. J Cleaner Prod. 2019;239:117946. https://doi.org/10.1016/j.jclepro.2019.117946
4. Liu F, Xie M, Yu G, Ke C, Zhao H. Study on calcination catalysis and the desilication mechanism for coal gangue. ACS Sustain Chem Eng. 2021;9(30):10318–25. https://doi.org/10.1021/acssuschemeng.1c03276
5. National Annual Report. Annual report on the prevention and control of solid waste pollution in large and medium-sized cities in 2020 (in Chinese). 2020
6. Stracher GB, Taylor TP. Coal fires burning out of control around the world: thermodynamic recipe for environmental catastrophe. Int J Coal Geol. 2004;59(1–2):7–17. https://doi.org/10.1016/j.coal.2003.03.002
7. Luo J, Fang Z, Smith RL. Ultrasound-enhanced conversion of biomass to biofuels. Prog Energy Combust Sci. 2014;41(1):56–93. https://doi.org/10.1016/j.pecs.2013.11.001
8. Tang Y, Wang H. Laboratorial investigation and simulation test for spontaneous combustion characteristics of the coal waste under lean-oxygen atmosphere. Combust Sci Technol. 2020;192(1):46–61. https://doi.org/10.1080/00102202.2018.1555821
9. Zhang Y, Ling TC. Reactivity activation of waste coal gangue and its impact on the properties of cement-based materials – a review. Constr Build Mater. 2020;234:117424. https://doi.org/10.1016/j.conbuildmat.2019.117424

10. Rodríguez J, Tobón J, Frías M, Sánchez de Rojas MI. Aprovechamiento de un residuo del carbón para reducción del impacto ambiental de la minería del carbón en Colombia: estudio del potencial de uso en la industria del cemento. Rev CINTEX. 2018;23(2):95–102. https://doi.org/10.33131/24222208.323

11. Long G, Li L, Li W, Ma K, Dong W, Bai C, et al. Enhanced mechanical properties and durability of coal gangue reinforced cement-soil mixture for foundation treatments. J Cleaner Prod. 2019;231:468–82. https://doi.org/10.1016/j.jclepro.2019.05.210

12. Zhang N, Li H, Liu X. Hydration mechanism and leaching behavior of bauxite-calcination-method red mud-coal gangue based cementitious materials. J Hazard Mater. 2016;314:172–80. https://doi.org/10.1016/j.jhazmat.2016.04.040

13. Nodehi M. A comparative review on foam-based versus lightweight aggregate-based alkali-activated materials and geopolymer. Innovative Infrastruct Solut. 2021;6(4):1–20. https://doi.org/10.1007/s41062-021-00595-w

14. Singh B, Ishwarya G, Gupta M, Bhattacharyya SK. Geopolymer concrete: a review of some recent developments. Constr Build Mater. 2015;85:78–90. https://doi.org/10.1016/j.conbuildmat.2015.03.036

15. Kuenzel C, Grover LM, Vandeperre L, Boccaccini AR, Cheeseman CR. Production of nepheline/quartz ceramics from geopolymer mortars. J Eur Ceram Soc. 2013;33(2):251–8. https://doi.org/10.1016/j.jeurceramsoc.2012.08.022

16. Liew Y-M, Heah C-Y, Li L, Jaya NA, Abdullah MMAB, Tan SJ, et al. Formation of one-part-mixing geopolymers and geopolymer ceramics from geopolymer powder. Constr Build Mater. 2017;156:9–18. https://doi.org/10.1016/j.conbuildmat.2017.08.110

17. Bernal SA, Bejarano J, Garzón C, Mejía De Gutiérrez R, Delvasto S, Rodríguez ED. Performance of refractory aluminosilicate particle/fiber-reinforced geopolymer composites. Composites, B: Eng. 2012;43(4):1919–28. https://doi.org/10.1016/j.compositesb.2012.02.027

18. Natali A, Manzi S, Bignozzi MC. Novel fiber-reinforced composite materials based on sustainable geopolymer matrix. Procedia Eng. 2011;21:1124–31. https://doi.org/10.1016/j.proeng.2011.11.2120

19. Ohno M, Li VC. A feasibility study of strain hardening fiber reinforced fly ash-based geopolymer composites. Constr Build Mater. 2014;57:163–8. https://doi.org/10.1016/j.conbuildmat.2014.02.005

20. Nodehi M, Taghvaee VM. Alkali-activated materials and geopolymer: a review of common precursors and activators addressing circular economy. Circ Econ Sustain. 2021;2(1):165–96. https://doi.org/10.1007/s43615-021-00029-w

21. Wang C, Xu G, Gu X, Gao Y, Zhao P. High value-added applications of coal fly ash in the form of porous materials: a review. Ceram Int. 2021;47(16):22302–15. https://doi.org/10.1016/j.ceramint.2021.05.070

22. Wen Q, Qu F, Yu Z, Graczyk-Zajac M, Xiong X, Riedel R. Si-based polymer-derived ceramics for energy conversion and storage. J Adv Ceram. 2022;11(2):197–246. https://doi.org/10.1007/s40145-021-0562-2

23. Liu J, Ren B, Wang Y, Lu Y, Wang L, Chen Y, et al. Hierarchical porous ceramics with 3D reticular architecture and efficient flow-through filtration towards high-temperature particulate matter capture. Chem Eng J. 2019;362(January):504–12. https://doi.org/10.1016/j.cej.2019.01.065

24. Dong B, Yang M, Wang F, Hao L, Xu X, Wang G, et al. Porous Al2O3 plates prepared by combing foaming and gel-tape casting methods for efficient collection of oil from water. Chem Eng J. 2019;370:658–65. https://doi.org/10.1016/j.cej.2019.03.218

25. Hlaváček P, Šmilauer V, Škvára F, Kopecký L, Šulc R. Inorganic foams made from alkali-activated fly ash: mechanical, chemical and physical properties. J Eur Ceram Soc. 2015;35(2):703–9. https://doi.org/10.1016/j.jeurceramsoc.2014.08.024

26. Novais RM, Buruberri LH, Ascensão G, Seabra MP, Labrincha JA. Porous biomass fly ash-based geopolymers with tailored thermal conductivity. J Cleaner Prod. 2016;119:99–107. https://doi.org/10.1016/j.jclepro.2016.01.083

27. Hemra K, Aungkavattana P. Effect of cordierite addition on compressive strength and thermal stability of metakaolin based geopolymer. Adv Powder Technol. 2016;27(3):1021–6. https://doi.org/10.1016/j.apt.2016.04.019

28. Novais RM, Buruberri LH, Seabra MP, Labrincha JA. Novel porous fly-ash containing geopolymer monoliths for lead adsorption from wastewaters. J Hazard Mater. 2016;318:631–40. https://doi.org/10.1016/j.jhazmat.2016.07.059

29. Onutai S, Kobayashi T, Thavorniti P, Jiemsirilers S. Porous fly ash-based geopolymer composite fiber as an adsorbent for removal of heavy metal ions from wastewater. Mater Lett. 2019;236:30–3. https://doi.org/10.1016/j.matlet.2018.10.035

30. Novais RM, Carvalheiras J, Tobaldi DM, Seabra MP, Pullar RC, Labrincha JA. Synthesis of porous biomass fly ash-based geopolymer spheres for efficient removal of methylene blue from wastewaters. J Cleaner Prod. 2019;207:350–62. https://doi.org/10.1016/j.jclepro.2018.09.265

31. Qiao Y, Li X, Bai C, Li H, Yan J, Wang Y, et al. Effects of surfactants/stabilizing agents on the microstructure and properties of porous geopolymers by direct foaming. J Asian Ceram Soc. 2021;9(1):412–23. https://doi.org/10.1080/21870764.2021.1873482

32. Bai C, Conte A, Colombo P. Open-cell phosphate-based geopolymer foams by frothing. Mater Lett. 2017;188:379–82. https://doi.org/10.1016/j.matlet.2016.11.103

33. Bai C, Colombo P. High-porosity geopolymer membrane supports by peroxide route with the addition of egg white as surfactant. Ceram Int. 2017;43(2):2267–73. https://doi.org/10.1016/j.ceramint.2016.10.205

34. Bai C, Franchin G, Elsayed H, Conte A, Colombo P. High strength metakaolin-based geopolymer foams with variable macroporous structure. J Eur Ceram Soc. 2016;36(16):4243–9. https://doi.org/10.1016/j.jeurceramsoc.2016.06.045

35. Kovářík T, Křenek T, Rieger D, Pola M, Říha J, Svoboda M, et al. Synthesis of open-cell ceramic foam derived from geopolymer precursor via replica technique. Mater Lett. 2017;209:497–500. https://doi.org/10.1016/j.matlet.2017.08.081

36. Rasouli HR, Golestani-Fard F, Mirhabibi AR, Nasab GM, MacKenzie KJD, Shahraki MH. Fabrication and properties of microporous metakaolin-based geopolymer bodies with polylactic acid (PLA) fibers as pore generators. Ceram Int. 2015;41(6):7872–80. https://doi.org/10.1016/j.ceramint.2015.02.125

37. Palmero P, Formia A, Antonaci P, Brini S, Tulliani JM. Geopolymer technology for application-oriented dense and

lightened materials. Elaboration and characterization. Ceram Int. 2015;41(10):12967–79. https://doi.org/10.1016/j.ceramint.2015.06.140

38. Franchin CP. Porous geopolymer components through inverse replica of 3D printed sacrificial templates. J Ceram Sci Technol. 2015;6(2):105–12. https://doi.org/10.4416/JCST2014-00057

39. Papa E, Medri V, Benito P, Vaccari A, Bugani S, Jaroszewicz J, et al. Insights into the macroporosity of freeze-cast hierarchical geopolymers. RSC Adv. 2016;6(29):24635–44. https://doi.org/10.1039/c6ra02232d

40. Xia M, Sanjayan J. Method of formulating geopolymer for 3D printing for construction applications. Mater Des. 2016;110:382–90. https://doi.org/10.1016/j.matdes.2016.07.136

41. Zhong J, Zhou GX, He PG, Yang ZH, Jia DC. 3D printing strong and conductive geo-polymer nanocomposite structures modified by graphene oxide. Carbon N Y. 2017;117:421–6. https://doi.org/10.1016/j.carbon.2017.02.102

42. Franchin G, Scanferla P, Zeffiro L, Elsayed H, Baliello A, Giacomello G, et al. Direct ink writing of geopolymeric inks. J Eur Ceram Soc. 2017;37(6):2481–9. https://doi.org/10.1016/j.jeurceramsoc.2017.01.030

43. Medpelli D, Seo JM, Seo DK. Geopolymer with hierarchically meso-/macroporous structures from reactive emulsion templating. J Am Ceram Soc. 2014;97(1):70–3. https://doi.org/10.1111/jace.12724

44. Gurbuz IB, Ozkan G. Consumers' knowledge, attitude and behavioural patterns towards the liquid wastes (cooking oil) in Istanbul, Turkey. Environ Sci Pollut Res. 2019;26(16):16529–36. https://doi.org/10.1007/s11356-019-05078-1

45. Awogbemi O, Kallon DV Von, Aigbodion VS, Panda S. Advances in biotechnological applications of waste cooking oil. Case Stud Chem Environ Eng. 2021;4:100158. https://doi.org/10.1016/j.cscee.2021.100158

46. Singh D, Sharma D, Soni SL, Inda CS, Sharma S, Sharma PK, et al. A comprehensive review of biodiesel production from waste cooking oil and its use as fuel in compression ignition engines: 3rd generation cleaner feedstock. J Cleaner Prod. 2021;307:127299. https://doi.org/10.1016/j.jclepro.2021.127299

47. Panadare DC, Rathod VK. Applications of waste cooking oil other than biodiesel: a review. Iran J Chem Eng. 2015;12(3):55–76.

48. Madhusudan C, Kasarapu V, Chittimadula M, Reddy YS, Reddy CV. Synthesis and characterization of Y and Dy co-doped ceria solid electrolytes for IT-SOFCs: a microwave sintering. Rare Met. 2021;40(11):3329–36. https://doi.org/10.1007/s12598-018-1059-1

49. Calles-Arriaga CA, López-Hernández J, Hernández-Ordoñez M, Echavarría-Solís RA, Ovando-Medina VM. Thermal characterization of microwave assisted foaming of expandable polystyrene. Ing Invest Tecnol. 2016;17(1):15–21. https://doi.org/10.1016/j.riit.2016.01.002

50. Minay EJ, Veronesi P, Cannillo V, Leonelli C, Boccaccini AR. Control of pore size by metallic fibres in glass matrix composite foams produced by microwave heating. J Eur Ceram Soc. 2004;24(10–11):3203–8. https://doi.org/10.1016/j.jeurceramsoc.2003.11.015

51. Chien YC. Field study of in situ remediation of petroleum hydrocarbon contaminated soil on site using microwave energy.

J Hazard Mater. 2012;199–200:457–61. https://doi.org/10.1016/j.jhazmat.2011.11.012

52. Jimenez GD, Monti T, Titman JJ, Hernandez-Montoya V, Kingman SW, Binner ER. New insights into microwave pyrolysis of biomass: preparation of carbon-based products from pecan nutshells and their application in wastewater treatment. J Anal Appl Pyrolysis. 2017;124:113–21. https://doi.org/10.1016/j.jaap.2017.02.013

53. John RS, Batchelor AR, Ivanov D, Udoudo OB, Jones DA, Dodds C, et al. Understanding microwave induced sorting of porphyry copper ores. Miner Eng. 2015;84:77–87. https://doi.org/10.1016/j.mineng.2015.10.006

54. Nadeem M, Ul Haq E, Ahmed F, Asif Rafiq M, Hameed Awan G, Zain-ul-Abdein M. Effect of microwave curing on the construction properties of natural soil based geopolymer foam. Constr Build Mater. 2020;230:117074. https://doi.org/10.1016/j.conbuildmat.2019.117074

55. Haq EU, Padmanabhan SK, Zubair M, Ali L, Licciulli A. Intumescence behaviour of bottom ash based geopolymer mortar through microwave irradiation – as affected by alkali activation. Constr Build Mater. 2016;126:951–6. https://doi.org/10.1016/j.conbuildmat.2016.08.135

56. Onutai S, Jiemsirilers S, Thavorniti P, Kobayashi T. Fast microwave syntheses of fly ash based porous geopolymers in the presence of high alkali concentration. Ceram Int. 2016;42(8):9866–74. https://doi.org/10.1016/j.ceramint.2016.03.086

57. Ul Haq E, Kunjalukkal Padmanabhan S, Licciulli A. Microwave synthesis of thermal insulating foams from coal derived bottom ash. Fuel Process Technol. 2015;130(C):263–7. https://doi.org/10.1016/j.fuproc.2014.10.017

58. Rashid M, Ul Haq E, Yousaf S, Javed M, Nadeem M, Aziz U, et al. Light weight low thermal conductive fly ash foams through microwave irradiation for insulative, agricultural and self-healing purposes. Mater Today Proc. 2021;47:S38–45. https://doi.org/10.1016/j.matpr.2020.04.682

59. Bai C, Ni T, Wang Q, Li H, Colombo P. Porosity, mechanical and insulating properties of geopolymer foams using vegetable oil as the stabilizing agent. J Eur Ceram Soc. 2018;38(2):799–805. https://doi.org/10.1016/j.jeurceramsoc.2017.09.021

60. Bai C, Franchin G, Elsayed H, Zaggia A, Conte L, Li H, et al. High-porosity geopolymer foams with tailored porosity for thermal insulation and wastewater treatment. J Mater Res. 2017;32(17):3251–9. https://doi.org/10.1557/jmr.2017.127

61. Wang L, An L, Zhao J, Shimai S, Mao X, Zhang J, et al. High-strength porous alumina ceramics prepared from stable wet foams. J Adv Ceram. 2021;10(4):852–9. https://doi.org/10.1007/s40145-021-0479-9

62. Luukkonen T, Sarkkinen M, Kemppainen K, Rämö J, Lassi U. Metakaolin geopolymer characterization and application for ammonium removal from model solutions and landfill leachate. Appl Clay Sci. 2016;119:266–76. https://doi.org/10.1016/j.clay.2015.10.027

63. Febrianto J, Kosasih AN, Sunarso J, Ju YH, Indraswati N, Ismadji S. Equilibrium and kinetic studies in adsorption of heavy metals using biosorbent: a summary of recent studies. J Hazard Mater. 2009;162(2–3):616–45. https://doi.org/10.1016/j.jhazmat.2008.06.042

64. El Alouani M, Alehyen S, El Achouri M, Taibi M. Removal of cationic dye – methylene blue- from aqueous solution by adsorption on fly ash-based geopolymer. J Mater Environ Sci. 2018;9(1):32–46. https://doi.org/10.26872/jmes.2018.9.1.5

65. Hertel T, Novais RM, Murillo Alarcón R, Labrincha JA, Pontikes Y. Use of modified bauxite residue-based porous inorganic polymer monoliths as adsorbents of methylene blue. J Cleaner Prod. 2019;227:877–89. https://doi.org/10.1016/j.jclepro.2019.04.084

66. Novais RM, Ascensão G, Tobaldi DM, Seabra MP, Labrincha JA. Biomass fly ash geopolymer monoliths for effective methylene blue removal from wastewaters. J Cleaner Prod. 2018;171:783–94. https://doi.org/10.1016/j.jclepro.2017.10.078

67. Kaya-Özkiper K, Uzun A, Soyer-Uzun S. Tuning adsorption, structure and compressive strength of sepiolite- and metakaolin-based alkali activated monoliths for methylene blue removal from waste water. Surf Interfaces. 2022;33(April):102110. https://doi.org/10.1016/j.surfin.2022.102110

68. Jin H, Zhang Y, Wang Q, Chang Q, Li C. Rapid removal of methylene blue and nickel ions and adsorption/desorption mechanism based on geopolymer adsorbent. Colloids Interface Sci Commun. 2021;45:100551. https://doi.org/10.1016/j.colcom.2021.100551

69. Bhuyan MAH, Gebre RK, Finnilä MAJ, Illikainen M, Luukkonen T. Preparation of filter by alkali activation of blast furnace slag and its application for dye removal. J Environ Chem Eng. 2022;10(1):107051. https://doi.org/10.1016/j.jece.2021.107051

70. Kaya-Özkiper K, Uzun A, Soyer-Uzun S. A novel alkali activated magnesium silicate as an effective and mechanically strong adsorbent for methylene blue removal. J Hazard Mater. 2022;424:127256. https://doi.org/10.1016/j.jhazmat.2021.127256

71. Dimas D, Giannopoulou I, Panias D. Polymerization in sodium silicate solutions: a fundamental process in geopolymerization technology. J Mater Sci. 2009;44(14):3719–30. https://doi.org/10.1007/s10853-009-3497-5

72. Frasson BJ, Pinto RCA, Rocha JC. Influence of different sources of coal gangue used as aluminosilicate powder on the mechanical properties and microstructure of alkali-activated cement. Mater Constr. 2019;69(336). https://doi.org/10.3989/mc.2019.12618

73. Musyarofah LND, Nurlaila R, Muwwaqor NF, Triwikantoro PS. Synthesis of high-purity zircon, zirconia, and silica nanopowders from local zircon sand. Ceram Int. 2019;45(6):6639–47. https://doi.org/10.1016/j.ceramint.2018.12.152

74. Hwang CL, Huynh TP. Effect of alkali-activator and rice husk ash content on strength development of fly ash and residual rice husk ash-based geopolymers. Constr Build Mater. 2015;101:1–9. https://doi.org/10.1016/j.conbuildmat.2015.10.025

75. Bossi A, Leofanti G, Moretti E, Giordano N. Morphological and structural effects of NaOH added to silica. J Mater Sci. 1973;8(8):1101–9. https://doi.org/10.1007/BF00632760

76. Horii N, Kuzuu N, Horikoshi H. Silica glass devitrification enhancement by a drop of sodium hydroxide saturated solution. Jpn J Appl Phys. 2020;59(SC):1–5. https://doi.org/10.7567/1347-4065/ab5166

77. Koshy N, Dondrob K, Hu L, Wen Q, Meegoda JN. Synthesis and characterization of geopolymers derived from coal gangue, fly ash and red mud. Constr Build Mater. 2019;206:287–96. https://doi.org/10.1016/j.conbuildmat.2019.02.076

78. Zhang W, Dong C, Huang P, Sun Q, Li M, Chai J. Experimental study on the characteristics of activated coal gangue and coal gangue-based geopolymer. Energies. 2020;13(10):2504. https://doi.org/10.3390/en13102504

79. Liu W, Liu W, Wang B, Duan H, Peng X, Chen X, et al. Novel hydroxy polyamine surfactant N-(2-hydroxyethyl)-N-dodecyl-ethanediamine: its synthesis and flotation performance study to quartz. Miner Eng. 2019;142(June):105894. https://doi.org/10.1016/j.mineng.2019.105894

80. Senthil Kumar R, Rajkumar P. Characterization of minerals in air dust particles in the state of Tamil Nadu, India through FTIR, XRD and SEM analyses. Infrared Phys Technol. 2014;67(2014):30–41. https://doi.org/10.1016/j.infrared.2014.06.002

81. Wang Y, Li J, Zhang W, Li P, Guo J, Yao K. Citric acid inhibits the floatability of quartz in the Mg^{2+} system. Physicochem Prob Miner Process. 2021;57(6):1–11. https://doi.org/10.37190/PPMP/142160

82. Cheng F, Cui L, Miller JD, Wang X. Aluminum leaching from calcined coal waste using hydrochloric acid solution. Miner Process Extr Metall Rev. 2012;33(6):391–403. https://doi.org/10.1080/08827508.2011.601700

83. Janik LJ, Keeling JL. FT-IR partial least-squares analysis of tubular halloysite in kaolin samples from the Mount Hope Kaolin Deposit. Clay Miner. 1993;28(3):365–78. https://doi.org/10.1180/claymin.1993.028.3.03

84. Yan S, Zhang F, Wang L, Rong Y, He P, Jia D, et al. A green and low-cost hollow gangue microsphere/geopolymer adsorbent for the effective removal of heavy metals from wastewaters. J Environ Manage. 2019;246(May):174–83. https://doi.org/10.1016/j.jenvman.2019.05.120

85. Huang G, Ji Y, Li J, Hou Z, Dong Z. Improving strength of calcinated coal gangue geopolymer mortars via increasing calcium content. Constr Build Mater. 2018;166:760–8. https://doi.org/10.1016/j.conbuildmat.2018.02.005

86. Yan S, He P, Jia D, Wang Q, Liu J, Yang J, et al. Synthesis of novel low-cost porous gangue microsphere/geopolymer composites and their adsorption properties for dyes. Int J Appl Ceram Technol. 2018;15(6):1602–14. https://doi.org/10.1111/ijac.13045

87. Gong C, Li D. Mineral composition variation of calcined coal gangue doped with calcium and fluorite. Kuei Suan Jen Hsueh Pao/J Chinese Ceram Soc. 2006;34(7):855–60. https://doi.org/10.14062/j.issn.0454-5648.2006.07.019

88. Zhang D, Wu S, Hu S, Zhou H, Tian D, Zhang S. Influence of calcination conditions on extracting aluminum oxide from coal gangue of Enshi Coalmine. Non-Met Mines. 2014;37(4):47–9. (in Chinese).

89. Zhou S, Dong J, Yu L, Xu C, Jiao X, Wang M. Effect of activated coal gangue in north China on the compressive strength and hydration process of cement. J Mater Civ Eng. 2019;31(4):04019022. https://doi.org/10.1061/1943-5533.0002643

90. Alehyen S, Achouri MEL, Taibi M. Characterization, microstructure and properties of fly ash-based geopolymer. J Mater Environ Sci. 2017;8(5):1783–96. https://www.jmaterenvironsci.com/%0A

91. Yan S, Zhang F, Liu J, Ren B, He P, Jia D, et al. Green synthesis of high porosity waste gangue microsphere/geopolymer

composite foams via hydrogen peroxide modification. J Cleaner Prod. 2019;227:483–94. https://doi.org/10.1016/j.jclepro.2019.04.185

92. Prud'homme E, Michaud P, Joussein E, Smith A, Peyratout C, Sobrados I, et al. Geomaterial foams: role assignment of raw materials in the network formation. J Sol-Gel Sci Technol. 2012;61(2):436–48. https://doi.org/10.1007/s10971-011-2644-z

93. Fernández-Jiménez A, Palomo A. Mid-infrared spectroscopic studies of alkali-activated fly ash structure. Microporous Mesoporous Mater. 2005;86(1–3):207–14. https://doi.org/10.1016/j.micromeso.2005.05.057

94. Granizo ML, Alonso S, Blanco-Varela MT, Palomo A. Alkaline activation of metakaolin: effect of calcium hydroxide in the products of reaction. J Am Ceram Soc. 2002;85(1):225–31. https://doi.org/10.1111/j.1151-2916.2002.tb00070.x

95. Phair JW, Van Deventer JSJ. Effect of the silicate activator pH on the microstructural characteristics of waste-based geopolymers. Int J Miner Process. 2002;66(1–4):121–43. https://doi.org/10.1016/S0301-7516(02)00013-3

96. Cilla MS, Morelli MR, Colombo P. Open cell geopolymer foams by a novel saponification/peroxide/gelcasting combined route. J Eur Ceram Soc. 2014;34(12):3133–7. https://doi.org/10.1016/j.jeurceramsoc.2014.04.001

97. Prud'homme E, Michaud P, Joussein E, Peyratout C, Smith A, Arrii-Clacens S, et al. Silica fume as porogent agent in geomaterials at low temperature. J Eur Ceram Soc. 2010;30(7):1641–8. https://doi.org/10.1016/j.jeurceramsoc.2010.01.014

98. Liguori B, Capasso I, Romeo V, D'Auria M, Lavorgna M, Caputo D, et al. Hybrid geopolymeric foams with diatomite addition: effect on chemico-physical properties. J Cell Plast. 2017;53(5):525–36. https://doi.org/10.1177/0021955x17695092

99. Dembovska L, Bajare D, Ducman V, Korat L, Bumanis G. The use of different by-products in the production of lightweight alkali activated building materials. Constr Build Mater. 2017;135:315–22. https://doi.org/10.1016/j.conbuildmat.2017.01.005

100. Murri AN, Medri V, Papa E, Laghi L, Mingazzini C, Landi E. Porous geopolymer insulating core from a metakaolin/biomass ash composite. Environments. 2017;4(4):1–13. https://doi.org/10.3390/environments4040086

101. Yan S, Zhang F, Wang S, He P, Jia D, Yang J. Crystallization behavior and mechanical properties of high open porosity dolomite hollow microspheres filled hybrid geopolymer foams. Cem Concr Compos. 2019;104(July):103376. https://doi.org/10.1016/j.cemconcomp.2019.103376

102. Lopez-Gil A, Silva-Bellucci F, Velasco D, Ardanuy M, Rodriguez-Perez MA. Cellular structure and mechanical properties of starch-based foamed blocks reinforced with natural fibers and produced by microwave heating. Ind Crops Prod. 2015;66:194–205. https://doi.org/10.1016/j.indcrop.2014.12.025

103. Hui KS, Chao CYH, Kot SC. Removal of mixed heavy metal ions in wastewater by zeolite 4A and residual products from recycled coal fly ash. J Hazard Mater. 2005;127(1–3):89–101. https://doi.org/10.1016/j.jhazmat.2005.06.027

104. Rożek P, Król M, Mozgawa W. Lightweight geopolymer-expanded glass composites for removal of methylene blue from aqueous solutions. Ceram Int. 2020;46(12):19785–91. https://doi.org/10.1016/j.ceramint.2020.05.011

105. Zhang Y, Liu L. Fly ash-based geopolymer as a novel photocatalyst for degradation of dye from wastewater. Particuology. 2013;11(3):353–8. https://doi.org/10.1016/j.partic.2012.10.007

106. Khan MI, Min TK, Azizli K, Sufian S, Ullah H, Man Z. Effective removal of methylene blue from water using phosphoric acid based geopolymers: synthesis, characterizations and adsorption studies. RSC Adv. 2015;5(75):61410–20. https://doi.org/10.1039/c5ra08255b

107. Li L, Wang S, Zhu Z. Geopolymeric adsorbents from fly ash for dye removal from aqueous solution. J Colloid Interface Sci. 2006;300(1):52–9. https://doi.org/10.1016/j.jcis.2006.03.062

108. Hameed BH. Spent tea leaves: a new non-conventional and low-cost adsorbent for removal of basic dye from aqueous solutions. J Hazard Mater. 2009;161(2–3):753–9. https://doi.org/10.1016/j.jhazmat.2008.04.019

109. Setiabudi HD, Jusoh R, Suhaimi SFRM, Masrur SF. Adsorption of methylene blue onto oil palm (*Elaeis guineensis*) leaves: process optimization, isotherm, kinetics and thermodynamic studies. J Taiwan Inst Chem Eng. 2016;63:363–70. https://doi.org/10.1016/j.jtice.2016.03.035

110. Ariharan A, Viswanathan B, Nandhakumar V. Nitrogen doped graphene as potential material for hydrogen storage. Graphene. 2017;06(02):41–60. https://doi.org/10.4236/graphene.2017.62004

111. Arenillas A, Pevida C, Rubiera F, Palacios JM, Navarrete R, Denoyel R, et al. Surface characterisation of synthetic coal chars made from model compounds. Carbon N Y. 2004;42(7):1345–50. https://doi.org/10.1016/j.carbon.2004.01.017

112. Buttersack C. Modeling of type IV and V sigmoidal adsorption isotherms. Phys Chem Chem Phys. 2019;21(10):5614–26. https://doi.org/10.1039/c8cp07751g

113. Su Q, Deng L, Ye Q, He Y, Cui X. KOH-activated geopolymer microspheres recycle Co(II) with higher adsorption capacity than NaOH-activated ones. ACS Omega. 2020;5(37):23898–908. https://doi.org/10.1021/acsomega.0c03158

114. Novais RM, Ascensão G, Tobaldi DM, Seabra MP, Labrincha JA. Biomass fly ash geopolymer monoliths for effective methylene blue removal from wastewaters. J Cleaner Prod. 2018;171:783–94. https://doi.org/10.1016/j.jclepro.2017.10.078

115. Kaewmee P, Song M, Iwanami M, Tsutsumi H, Takahashi F. Porous and reusable potassium-activated geopolymer adsorbent with high compressive strength fabricated from coal fly ash wastes. J Cleaner Prod. 2020;272:122617. https://doi.org/10.1016/j.jclepro.2020.122617

116. Wang X, Li X, Bai C, Qiao Y, Li H, Zhang L, et al. Facile synthesis of porous geopolymers via the addition of a water-soluble pore forming agent. Ceram Int. 2021;48(2):2853–64. https://doi.org/10.1016/j.ceramint.2021.10.075

117. Hermann DT, Tome S, Shikuku VO, Tchuigwa JB, Spieß A, Janiak C, et al. Enhanced performance of hydrogen peroxide modified pozzolan-based geopolymer for abatement of methylene blue from aqueous medium. Silicon. 2022;14:5191–206. https://doi.org/10.1007/s12633-021-01264-4

118. Dzoujo HT, Shikuku VO, Tome S, Akiri S, Kengne NM, Abdpour S, et al. Synthesis of pozzolan and sugarcane bagasse derived geopolymer-biochar composites for methylene blue sequestration from aqueous medium. J Environ Manage. 2022;318(7):115533. https://doi.org/10.1016/j.jenvman.2022.115533

119. Al-Ghouti MA, Khan M, Nasser MS, Al Saad K, Heng OE. Application of geopolymers synthesized from incinerated municipal solid waste ashes for the removal of cationic dye from water. PLoS One. 2020;15(11):e0239095. https://doi.org/10.1371/journal.pone.0239095

SUPPORTING INFORMATION

Additional supporting information can be found online in the Supporting Information section at the end of this article.